ADVANCED MATERIALS
www.advmat.de

Electrosynthesis of Hydrogen Peroxide Synergistically Catalyzed by Atomic Co–N_x–C Sites and Oxygen Functional Groups in Noble-Metal-Free Electrocatalysts

*Bo-Quan Li, Chang-Xin Zhao, Jia-Ning Liu, and Qiang Zhang**

Hydrogen peroxide (H_2O_2) is a green oxidizer widely involved in a vast number of chemical reactions. Electrochemical reduction of oxygen to H_2O_2 constitutes an environmentally friendly synthetic route. However, the oxygen reduction reaction (ORR) is kinetically sluggish and undesired water serves as the main product on most electrocatalysts. Therefore, electrocatalysts with high reactivity and selectivity are highly required for H_2O_2 electrosynthesis. In this work, a synergistic strategy is proposed for the preparation of H_2O_2 electrocatalysts with high ORR reactivity and high H_2O_2 selectivity. A Co–N_x–C site and oxygen functional group comodified carbon-based electrocatalyst (named as Co–POC–O) is synthesized. The Co–POC–O electrocatalyst exhibits excellent catalytic performance for H_2O_2 electrosynthesis in O_2-saturated 0.10 M KOH with a high selectivity over 80% as well as very high reactivity with an ORR potential at 1 mA cm^{-2} of 0.79 V versus the reversible hydrogen electrode (RHE). Further mechanism study identifies that the Co–N_x–C sites and oxygen functional groups contribute to the reactivity and selectivity for H_2O_2 electrogeneration, respectively. This work affords not only an emerging strategy to design H_2O_2 electrosynthesis catalysts with remarkable performance, but also the principles of rational combination of multiple active sites for green and sustainable synthesis of chemicals through electrochemical processes.

Hydrogen peroxide (H_2O_2) constitutes one of the 100 most important chemicals that is widely ultilized in multiple chemical processes including paper manufacturing, pharmaceutical production, and waste degradation,[1] where H_2O_2 serves as an ideal environmental friendly oxidant that only generates water as the byproduct.[2] The enormous and rapidly increasing demand of H_2O_2 globally starves for sufficient, inexpensive, and environmental friendly technologies for massive H_2O_2 production. Currently, the industrial manufacture of H_2O_2 applies the anthraquinone oxidation/reduction technology. The anthraquinone technology starts with hydrogen and oxygen and involves a series of processes including oxidation, hetrogenenation, drying, and extracting. This multiple-step procedure requires complex chemical plants with many reactors and separation equipment, consumes a huge amount of energy, and generates a considerable amount of waste chemicals along with many safety issues.[3] These disadvantages render the current anthraquinone technology neither energy efficient nor environmental friendly, deviating from our pursuit for green chemistry.[4]

With the widespread use of electricity harvest from renewable energy, electrosynthesis of chemicals are strongly considered recently.[5] Compared with the current anthraquinone technology, direct electrochemical reduction of oxygen (the oxygen reduction reaction, ORR) affords an alternative approach to synthesis H_2O_2. Concretely, oxygen is electrochemically reduced to H_2O_2 through a two-electron pathway in alkaline aqueous electrolyte at room temperature.[6] Such electrochemical approach uses oxygen and water as the feedstocks and only produces hydroxyl as the byproduct, indicating the intrinsic environmental friendliness and high atomic efficiency. In addition, the two-electron ORR approach for H_2O_2 electrosynthesis renders better safety, low cost, and easy operation at mild conditions. Therefore, electrochemical synthesis of H_2O_2 is strongly considered.[1a,7]

Despite the advantages of the electrochemical synthesis of H_2O_2, the reduction of oxygen is highly sluggish in kinetics. High overpotential for oxygen reduction severely limits the energy efficiency of H_2O_2 electrosynthesis.[8] More importantly, there is a competitive four-electron pathway of oxygen reduction to undesired water. The competitive side reaction further reduces the yield of H_2O_2 with a low Coulombic efficiency.[6b,9] Therefore, it is of great significance to search electrocatalysts with high reactivity for ORR and high selectivity to generate H_2O_2.

Noble-metal-based electrocatalysts, such as platinum–mercury alloys,[10] demonstrate satisfactory performance but are impeded from their high toxicity and earth scarcity.[11] Meanwhile, carbon-based electrocatalysts and conducting polymers emerge as promising candidates for the electrosynthesis of H_2O_2 because of their high electronic conductivity, earth abundance, mechanical and chemical stability, and versatility in composition and structure.[12] Heteroatom doping,[13] defect

B.-Q. Li, C.-X. Zhao, J.-N. Liu, Prof. Q. Zhang
Beijing Key Laboratory of Green Chemical
Reaction Engineering and Technology
Department of Chemical Engineering
Tsinghua University
Beijing 100084, China
E-mail: zhang-qiang@mails.tsinghua.edu.cn

The ORCID identification number(s) for the author(s) of this article can be found under https://doi.org/10.1002/adma.201808173.

DOI: 10.1002/adma.201808173

engineering,[14] and fabrication of atomically dispersed M–N_x–C sites (M is a transition metal atom)[15] have been intensively investigated as effective strategies to improve the ORR reactivity of carbon-based H_2O_2 electrocatalysts. Very recently, oxygen functional groups (OFGs) are identified to sufficiently promote the selectivity for H_2O_2 electrochemical synthesis through the two-electron pathway.[9,16] Oxidative acid treatment[16,17] and many other methods[16a,18] are employed to modify nanocarbon with OFGs. However, high ORR reactivity and high H_2O_2 selectivity have rarely been simultaneously achieved. The electrocatalysts with high ORR reactivity usually afford the dominant four-electron pathway to generate water while the electrocatalysts with high H_2O_2 selectivity suffer from high overpotentials and limited current densities in most cases.[19] Therefore, there remains a great challenge in the fabrication of electrocatalysts with both high ORR reactivity and high H_2O_2 selectivity. Rational design and precise synthesis of H_2O_2 electrocatalysts with high reactivity and high selectivity are highly requested.

In this contribution, a Co–N_x–C site and oxygen functional group comodified carbon-based electrocatalyst (named as Co–POC–O) is proposed to electrosynthesize H_2O_2 with high reactivity and high selectivity. Atomic Co–N_x–C sites prove to be effective in many cases to reduce oxygen in aqueous electrolyte.[15b,20] Nevertheless, such motif lacks the selectivity for H_2O_2 generation that oxygen feedstocks are usually reduced to water through the four-electron pathway instead of desired H_2O_2 (**Figure 1**a).[21] Modification of OFGs on nanocarbon prominently promotes the selectivity for the two-electron ORR pathway to generate H_2O_2. However, OFGs exhibit limited capability to improve the kinetics for ORR with high overpotential and reduced H_2O_2 output (Figure 1b), and consequently, require the assistance of additional active sites with high ORR reactivity. Based on the above consideration, comodification of atomic Co–N_x–C sites and OFGs affords a feasible strategy to endow noble-metal-free electrocatalysts with high reactivity and high selectivity for H_2O_2 electrosynthesis. Atomic Co–N_x–C sites serve as active sites for oxygen reduction and OFGs promote the selectivity of the two-electron pathway (Figure 1c). We found that atomic Co–N_x–C sites and OFGs function synergistically to render the Co–POC–O electrocatalysts with high H_2O_2 selectivity of ≈80% with a wide potential range, high reactivity to afford an ORR potential at 1 mA cm^{-2} of 0.79 V versus RHE, a small Tafel slope of 34 mV $decade^{-1}$, and a high stability for 10.0 h, which is much better than most of the reported H_2O_2 electrocatalysts. The rational combination of multiple active sites into 3D interconnected conductive hosts is an emerging strategy for sustainable production of essential chemicals.

The comodification of atomic Co–N_x–C sites and OFGs was performed by pyrolysis of the predesigned precursor and following oxidative acid treatment. Cobalt-coordinated framework porphyrin (Co–POF) was selected as the pyrolysis precursor because the covalently linked cobalt-coordinated porphyrin not only shares similar chemical structure with Co–N_x–C sites, but also possesses intrinsically ordered framework structure with uniformly dispersed cobalt contents. Co–POF was one-pot synthesized following the direct synthesis methodology using benzene-1,4-dicarboxaldehyde and pyrrole as the building blocks and cobalt acetate as the cobalt source, respectively. Unfortunately, pure Co–POF tends to aggregate into dense spheres with a diameter of several micrometers (Figure S1, Supporting Information). This aggregated morphology is not favorable for the fabrication of atomic Co–N_x–C sites. Therefore, graphene (shortened as G) was introduced as the template to regulate the morphology of Co–POF for its uniform distribution. The morphology of the as-synthesized Co–POF with G template was characterized by scanning electron microscopy (SEM) and transmission electron microscopy (TEM). Compared with bare G (Figure S2, Supporting Information), Co–POF exhibits a homogeneous layered morphology of encapsulated graphene (**Figure 2**a; Figure S3, Supporting Information). According to the Fourier-transformed infrared spectrometry (FTIR) results, the adsorption band of the carbonyl group in BDA at 1700 cm^{-1} is significantly reduced in Co–POF, demonstrating the full conversion of BDA precursors into the desirable structure (Figure S4, Supporting Information). Compared with the X-ray diffraction (XRD) patterns of G, Co–POF exhibits a distinct diffraction peat at 13°, suggesting the intrinsically ordered framework structure of Co–POF (Figure S5, Supporting Information).[22]

The elemental composition of Co–POF was analyzed using X-ray photoelectron spectroscopy (XPS). Co–POF demonstrates a reasonable nitrogen content of 10.1 at% and a detectable cobalt content of 0.7 at%, while the nitrogen and cobalt contents of G are negligible (Figure S6a, Supporting Information). High-resolution cobalt 2p XPS spectrum (Figure S6b, Supporting Information) demonstrates the Co $2p_{3/2}$ and Co $2p_{1/2}$ spin–orbit peaks at 780.0 and 795.5 eV, respectively. These signals indicate that the cobalt content of Co–POF is in 2+ oxidation state.[23] Further high-resolution nitrogen 1s XPS spectrum of Co–POF is deconvoluted into Co–N at 399.3 eV and pyrrole N at 400.1 eV, implying cobalt ions are successfully coordinated within the porphyrin units as desired precursors to fabricate atomic Co–N_x–C sites (Figure 2b).[19,24]

The Co–POF with well-constructed Co–N linking was pyrolyzed at 950 °C under argon protection for the fabrication of atomic Co–N_x–C sites within nanocarbon. The pyrolysis product is named as Co–POC. SEM and TEM images (Figure 2c; Figure S7, Supporting Information) reveal a porous morphology of Co–POC with nanoparticles inside the pores.

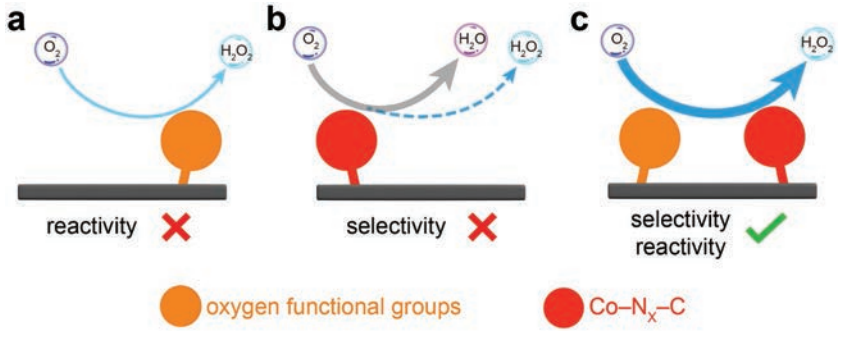

Figure 1. Schematic of the synergistic strategy of atomic Co–N_x–C sites and oxygen functional groups for H_2O_2 electrosynthesis on noble-metal-free electrocatalysts.

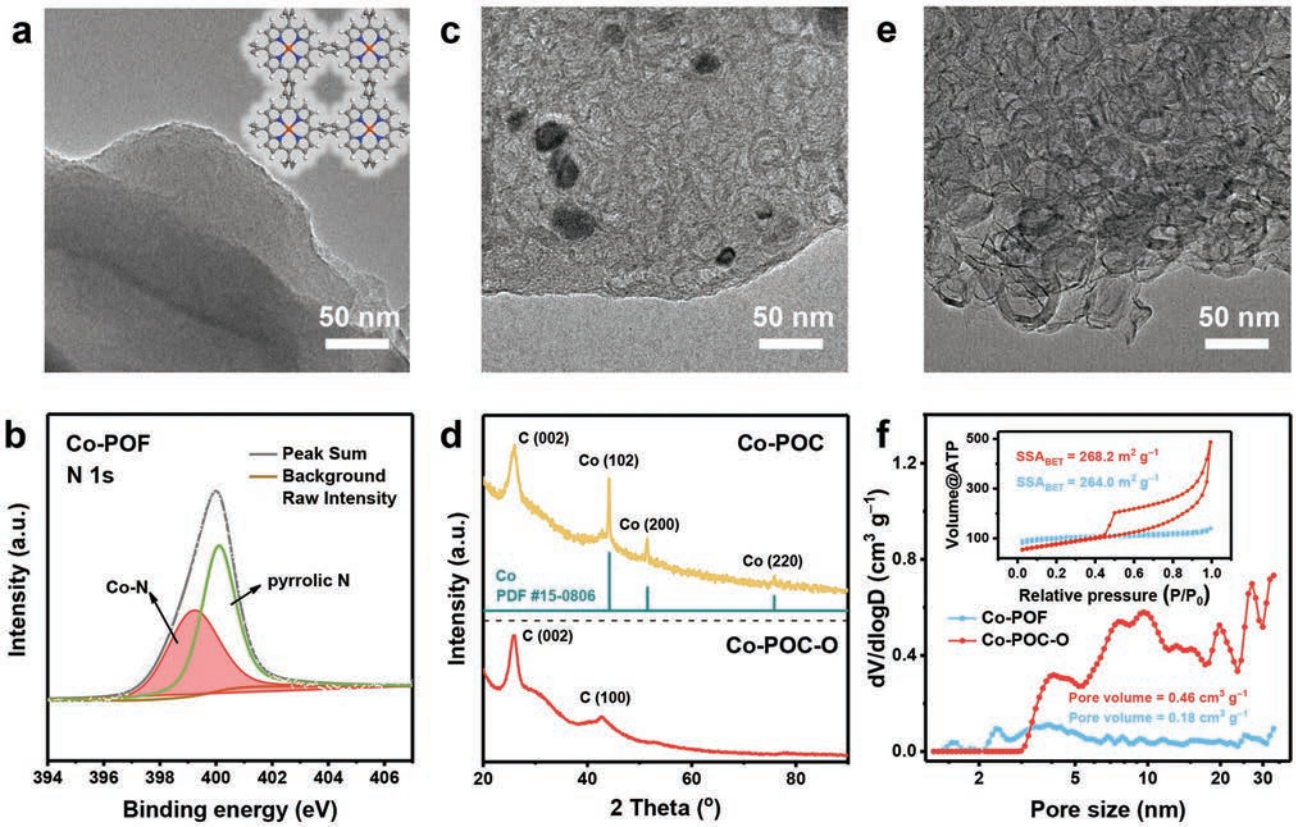

Figure 2. The fabrication of Co–POC–O from the Co–POF precursor. a) TEM image and b) high-resolution nitrogen 1s XPS spectrum of Co–POF. The inset in (a) shows the chemical structure of Co–POF. c) TEM image of Co–POC. d) XRD patterns of Co–POC and Co–POC–O. e) TEM image of Co–POC–O. f) N_2 isotherms and corresponding pore size distribution of Co–POC–O and Co–POF.

The inner diameters of the pores are approximately 20 nm. The XRD patterns of Co–POC exhibit an intense diffraction peak at 26° ascribed to crystallized carbon generated during the pyrolysis process and three sharp peaks at 44°, 51°, and 76° corresponding to the (111), (200), and (220) facets of metallic cobalt (PDF#15-0806), respectively (Figure 2d). The formation of metallic cobalt suggests that some coordinated cobalt ions are reduced under reductive atmosphere and aggregated into cobalt nanoparticles during the pyrolysis process. The cobalt nanoparticles facilitate the porous structure of Co–POC. Elemental analysis of Co–POC using XPS demonstrates a slightly reduced cobalt content of 0.6 at% compared with Co–POF as shown in Figure S8a (Supporting Information). Additionally, the high-resolution nitrogen 1s XPS spectrum of Co–POC affords the Co–N_x–C signal at 399.3 eV, suggesting atomically dispersed cobalt can be stabilized by surrounding carbon and nitrogen and partially preserved in Co–POC during pyrolysis (Figure S8b, Supporting Information).

Pyrolysis of the Co–POF precursor into porous Co–POC generates atomic Co–N_x–C sites for ORR electrocatalysis but is accompanied with element cobalt. In addition, OFGs are still required as active sites for selective H_2O_2 electrochemical generation. Based on the above consideration, Co–POC was further treated with nitric acid to simultaneously fabricate OFGs and remove bulk Co nanoparticles. The product after surface oxidization was named as Co–POC–O which was directly employed as the electrocatalyst for H_2O_2 electrosynthesis. The XRD patterns of Co–POC–O afford an intensive diffraction peak at 26° assigned to the (002) lattice face of crystallized carbon, indicating the carbon skeleton is well preserved during acid treatment (Figure 2d). More importantly, the XRD peaks of metallic cobalt are disappeared without the formation of other cobalt species, such as cobalt hydroxides or oxides. This result indicates metallic cobalt was fully dissolved by acid treatment. SEM and TEM images of Co–POC–O demonstrate the morphology of porous carbon without cobalt nanoparticles, further confirming the thorough removal of metallic cobalt to leave atomic Co–N_x–C active sites (Figure S9, Supporting Information). The diameter of the pores in Co–POC–O is estimated to be around 20 nm (Figure 2e), in agreement with the size of the cobalt nanoparticles in Co–POC. Therefore, the cobalt nanoparticles are inferred to contribute to the formation of the mesopores of Co–POC–O at high temperature.[25]

The porosity of Co–POC–O was further quantificationally evaluated based on the nitrogen adsorption/desorption isotherms. Compared with the Co–POF precursor, Co–POC–O exhibits typical type-IV patterns with an obvious hysteretic loop according to the IUPAC classification (Figure 2f), validating the unique mesoporous structure of Co–POC–O. The specific surface area of Co–POC–O is 268.2 m^2 g^{-1} using the multipoint Brunauer–Emmett–Teller (BET) method. The pore size distribution was determined according to the quenched solid

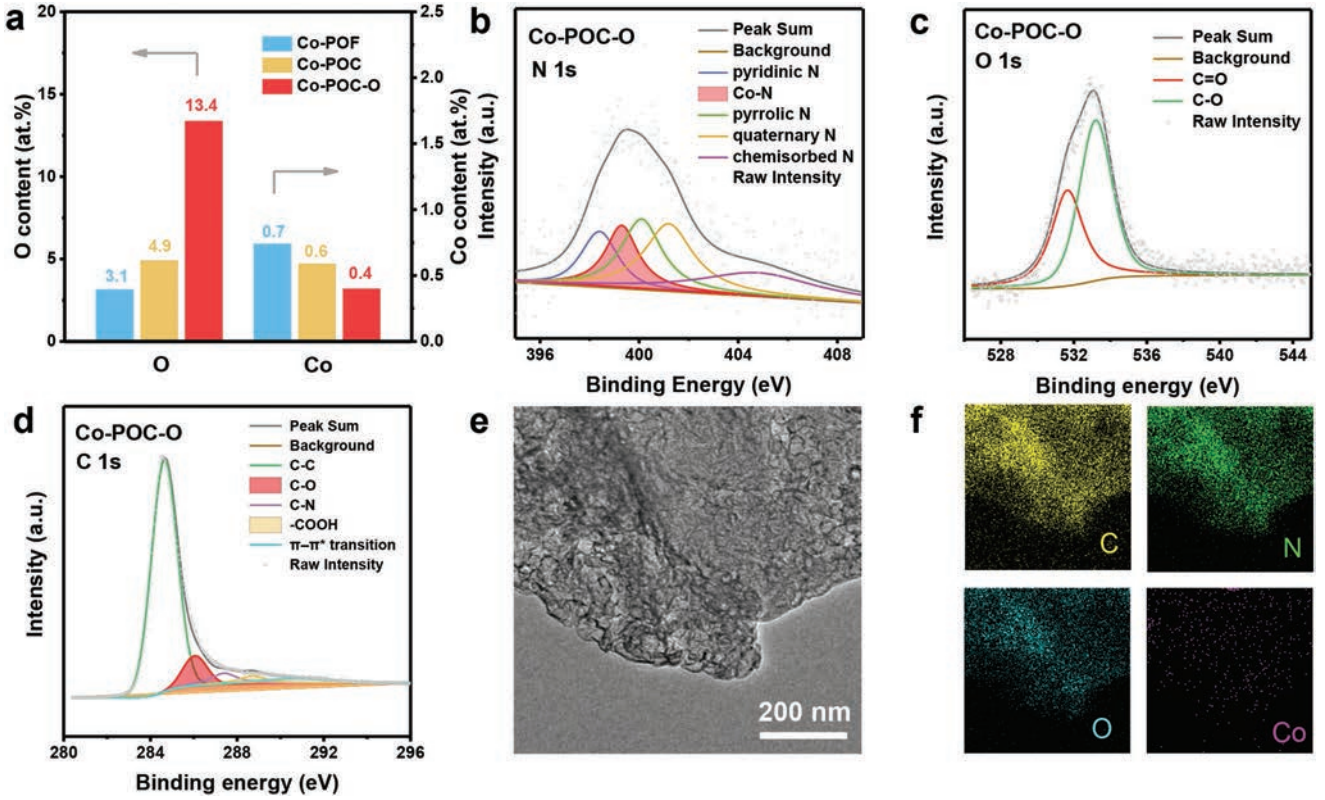

Figure 3. Material characterization of Co–POC–O. a) Element analysis of Co–POF, Co–POC, and Co–POC–O based on XPS measurements. b–d) High-resolution nitrogen 1s (b), oxygen 1s (c), and carbon 1s (d) XPS spectra of Co–POC–O. e) TEM image and f) corresponding EDS mapping of carbon, nitrogen, oxygen, and cobalt.

density function theory (DFT) model. As expected, Co–POC–O features abundant mesopores and higher pore volume of 0.46 $cm^3\ g^{-1}$ than the Co–POF precursor of 0.18 $cm^3\ g^{-1}$, which are favorable for heterogeneous oxygen electrocatalysis.

The comodification of atomic Co–N_x–C sites and OFGs on Co–POF–O was investigated using XPS. Co–POC–O demonstrates a comparable nitrogen content of 2.5 at% and slightly lower cobalt content of 0.4 at% compared with Co–POC, respectively (**Figure 3**a; Figure S10, Supporting Information). Considering there is no metallic cobalt in Co–POC–O according to the XRD and TEM characterization, we can infer that the cobalt element is atomically dispersed within the carbon skeleton to form atomic Co–N_x–C sites.[20a] High-resolution nitrogen 1s XPS spectrum of Co–POC–O further reveals the existence of Co–N interactions at 399.3 eV (Figure 3b). The detectable cobalt content and XPS Co–N signals unambiguously identify the fabrication of atomically dispersed Co–N_x–C sites in Co–POC–O for ORR electrocatalysis.

On the other hand, Co–POC–O exhibits a remarkable increase of oxygen content (13.4 at%) over Co–POC after oxidative acid treatment (Figure 3a). The intense oxygen peak in the XPS survey spectrum of Co–POC–O implies successful fabrication of OFGs (Figure S10, Supporting Information). High-resolution oxygen 1s XPS spectrum of Co–POC–O affords deconvoluted signals of oxygen doubly bonded to carbon (C=O, 40.7 at%) at 531.6 eV and oxygen singly bonded to carbon (C—O, 59.3 at%) at 533.2 eV serving as the dominant species of OFGs (Figure 3c).[26] Further deconvoluted high-resolution carbon 1s XPS validates the OFGs with bands of carbon in graphite (C—C, 76.2 at%) at 284.5 eV, carbon singly bound to oxygen (C—O, 9.3 at%) at 286.1 eV, carbon singly bound to nitrogen (C—N, 5.8 at%) at 287.4 eV, carbon bound to two oxygens (—COOH, 4.4 at%) at 288.7 eV and the characteristic shakeup line of carbon in aromatic compounds (π–π^* transition, 4.2 at%) at 290.5 eV (Figure 3d).[27] Therefore, the OFGs in Co–POC–O are identified as C—O, C=O, and —COOH. Further elemental mapping using energy-dispersive X-ray spectrometer (EDS) in Figure 3f demonstrates the uniform distribution of carbon, nitrogen, oxygen, and cobalt. The above characterization provides solid evidence for the comodification atomic Co–N_x–C sites and OFGs in the Co–POC–O electrocatalyst.

The co-existence of Co–N_x–C sites and OFGs in Co–POC–O encourages further electrochemical evaluation of applying Co–POC–O as an electrocatalyst for H_2O_2 electrosynthesis. The electrochemical performance was tested using a three-electrode system in oxygen-saturated 0.10 M KOH aqueous solution at room temperature. The working electrode was a rotating ring-disk electrode (RRDE) where ORR takes place at the disk electrode while the in situ generated H_2O_2 is successively oxidized at the ring electrode. The rotating speed was 1600 rpm. The electrocatalysts were first homogeneously dispersed in ethanol with Nafion as the binder and then deposited on the prepolished disk electrode of the RRDE, which was then directly used in electrochemical measurements. The areal loading was 0.10 mg cm^{-2} for all the samples.

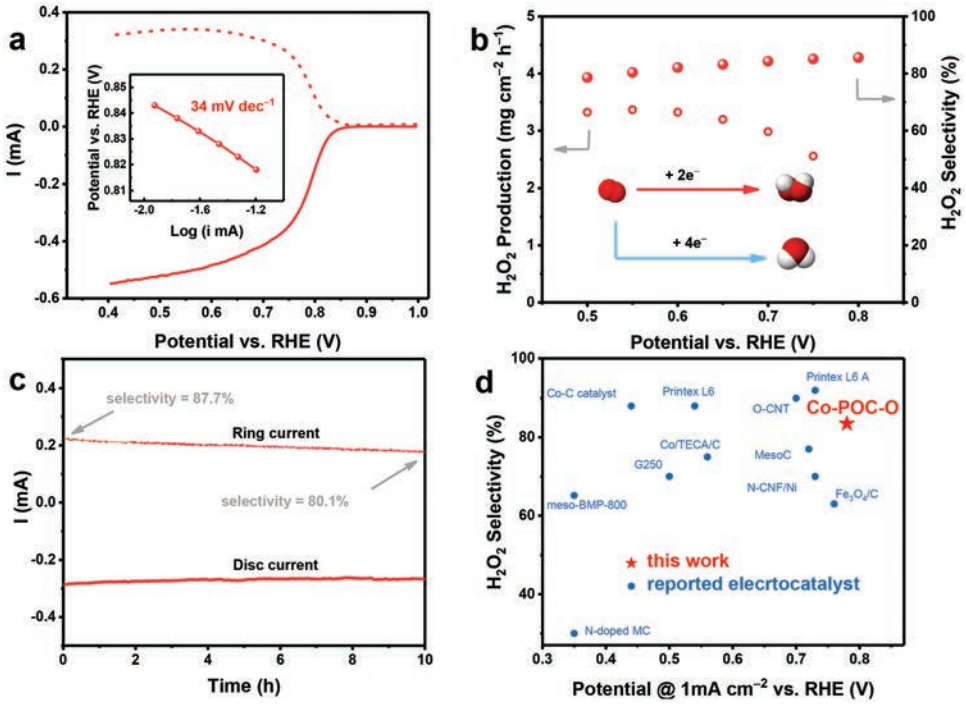

Figure 4. Electrosynthesis of H_2O_2 on the noble-metal-free Co–POC–O electrocatalyst in O_2-saturated 0.10 M KOH electrolyte. a) 95% *iR*-compensated LSV profiles of Co–POC–O at a scan rate of 10.0 mV s^{-1}. The inset in (a) shows the corresponding Tafel plots. b) H_2O_2 productivity and selectivity on the noble-metal-free Co–POC–O electrocatalyst. c) Chronoamperometric response of the Co–POC–O electrocatalyst for stability evaluation. d) Comparison of the reactivity and selectivity for H_2O_2 electrosynthesis on Co–POC–O and other reported electrocatalysts.

Figure 4a demonstrates the linear sweep voltammetry (LSV) profiles of the Co–POC–O electrocatalyst. The disk current (i_d, solid line) represents the ORR current while the ring current (i_r, dashed line) monitors H_2O_2 production. The Co–POC–O electrocatalyst exhibits high reactivity for oxygen reduction to render an onset potential of 0.84 V versus the reversible hydrogen electrode (RHE). The potential required to reach the current density of 1.0 mA cm^{-2} is 0.78 V versus RHE, which is much improved than the previously reported results (Figure 4d). Moreover, the Tafel slope of Co–POC–O is 34 mV decade^{-1}, suggesting rapid kinetics of oxygen reduction on the Co–POC–O electrocatalyst.

Figure 4b exhibits the productivity and selectivity for H_2O_2 electrosynthesis using the Co–POC–O electrocatalyst based on the data in Figure 4a. Evidently, high selectivity around 80% was achieved with a potential range from 0.50 to 0.80 V versus RHE, indicating that ORR on the Co–POC–O electrocatalyst goes through the dominated two-electron pathway with H_2O_2 as the final product. Specifically, Co–POC–O affords the H_2O_2 selectivity of 85.6% at the current density of 1.0 mA cm^{-2}, superior than many other reported electrocatalysts (Figure 4d).[9,13b,d,14b,16,28] The high ORR reactivity and high selectivity for the two-electron process render Co–POC–O as an excellent noble-metal-free electrocatalyst for H_2O_2 electrosynthesis. Consequently, high-sufficient H_2O_2 production was accomplished. For instance, Co–POC–O achieves a H_2O_2 output of 2.98 mg cm^{-2} h^{-1} at the potential of 0.70 V versus RHE. Long-term durability was evaluated according to the chronoamperometric responses. Co–POC–O maintains 82.8% and 92.7% of the ring and the disk current under continuous H_2O_2 production for 10.0 h, respectively (Figure 4c). The negligible decrease of the current density indicates the structural stability of active sites under working conditions for robust electrochemical production. By comodifying atomic Co–N_x–C sites and OFGs, Co–POC–O renders an impressive performance in reactivity, selectivity, and stability, highly desired as superb electrocatalysts for green and sustainable H_2O_2 electrosynthesis.

In order to identify the synergy between atomic Co–N_x–C sites and OFGs that contribute simultaneously to the high performance of H_2O_2 electrosynthesis, further mechanism investigation was carried out. Control samples were designed with only one category of active sites (for either ORR reactivity or H_2O_2 selectivity) but identical in other aspects. Concretely, electrocatalysts with atomic Co–N_x–C sites but without OFGs (named as Co–POC–R) and electrocatalysts with OFGs but without atomic Co–N_x–C sites (named as POC–O) were fabricated and characterized in regard to morphology, composition, and electrochemical performance.

The fabrication of Co–POC–R was otherwise identical as Co–POC–O except treating Co–POC with nonoxidative hydrochloric acid instead of oxidative nitric acid. Co–POC–R shares similar mesoporous and cobalt nanoparticle–free morphology as Co–POC–O verified by SEM and TEM images in Figure S11 (Supporting Information) and XRD patterns in Figure S12 (Supporting Information). The specific surface area of Co–POC–R (268.6 m^2 g^{-1}) is also comparable with Co–POC–O with similar pore volume and pore size distribution evaluated using the same methods (Figure S13, Supporting Information). The XPS survey spectrum of Co–POC–R demonstrates a much lower oxygen content of 2.0 at% but similar cobalt content of 0.3 at%

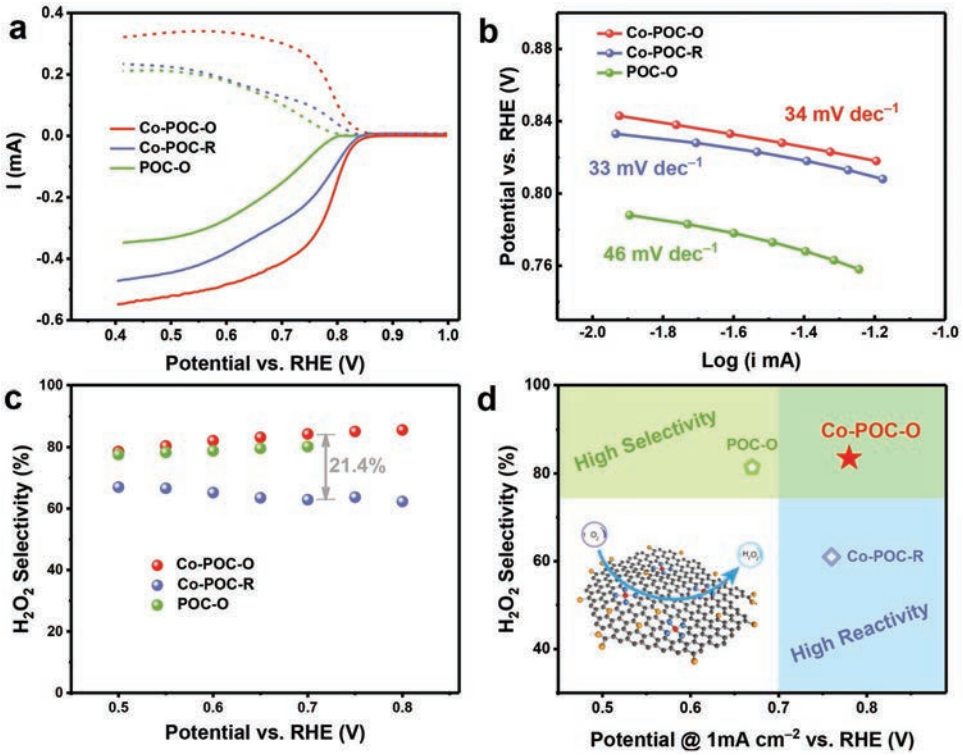

Figure 5. Mechanistic investigation on the noble-metal-free Co–POC–O electrocatalyst. a) 95% *iR*-compensated LSV profiles at a scan rate of 10.0 mV s^{-1}, b) corresponding Tafel plots, and c) H_2O_2 selectivity of Co–POC–O, Co–POC–R, and POC–O electrocatalysts. d) Performance comparison in regard to reactivity and selectivity for H_2O_2 electrosynthesis on Co–POC–O, Co–POC–R, and POC–O electrocatalysts. The inset in (d) shows the mechanism scheme for synergistic H_2O_2 electrosynthesis. The carbon, nitrogen, oxygen, and cobalt atoms are marked with black, blue, yellow, and red, respectively.

compared with Co–POC–O (Figure S14a, Supporting Information). Furthermore, the Co–N interaction can be clearly identified according to the high-resolution nitrogen 1s XPS spectrum of Co–POC–R, indicating the Co–N_x–C sites are inherited (Figure S14b, Supporting Information). Based on the above discussion, Co–POC–R is exclusively fabricated with Co–N_x–C sites but without OFGs, serving an ideal control sample for mechanism investigation.

The electrochemical performance of Co–POC–O was evaluated using the same method as Co–POC–O. As expected, the Co–POC–R electrocatalyst exhibits similar ORR reactivity with the potential at 1.0 mA cm^{-2} being 0.76 V versus RHE and the Tafel slope of 33 mV $decade^{-1}$ as Co–POC–O (**Figure 5**a,b). However, the selectivity of Co–POC–R is significantly decreased during H_2O_2 electrochemical production (Figure 5c). At the potential of 0.70 V, the H_2O_2 selectivity of Co–POC–R is 21.4% less than that of Co–POC–O. Considering similar Co–N_x–C sites and the absence of OFGs, the loss in selectivity is mainly attributed to the absence of OFGs in Co–POC–R. Therefore, Co–N_x–C active sites promote the ORR reactivity for H_2O_2 electrosynthesis but require the assistance of OFGs for the selective two-electron reduction.

On the other hand, POC–O with OFGs but without atomic Co–N_x–C sites was fabricated following otherwise identical procedures as Co–POC–O except using the cobalt-free precursors. Accordingly, framework porphyrin (named as POF) serves as the cobalt-free precursor for pyrolysis and oxidative acid treatment. POF was prepared following the synthetic method of Co–POF without the introduction of any cobalt source. The layered sheet morphology of POF resembles that of Co–POF according to the SEM and TEM images (Figure S15, Supporting Information). XPS measurements of POF exhibit a reasonable nitrogen content of 11.0 at% (Figure S16a, Supporting Information). High-resolution nitrogen 1s XPS spectrum further demonstrates pyrrolic N as the dominant nitrogen species, which is consistent with the molecular structure of POF (Figure S16b, Supporting Information).

POC–O was obtained after pyrolysis of POF at 950 °C and following oxidation with nitric acid. As shown in Figure S17 (Supporting Information), POC–O remains the layered morphology as Co–POC–O. POC–O also exhibits a comparable surface area (240.5 m^2 g^{-1}), pore volume (0.36 cm^3 g^{-1}), and pore size distribution as Co–POC–O (Figure S18, Supporting Information). The nitrogen and oxygen content of POC–O are 3.2 at% and 23.3 at% according to the XPS survey spectrum, respectively, with similar tendency as Co–POC–O (Figure S19a, Supporting Information). High-resolution nitrogen 1s XPS spectrum of POC–O affords no Co–N species in agreement with the cobalt-free POF precursor (Figure S19b, Supporting Information). Nevertheless, high-resolution oxygen 1s XPS spectrum of Co–POC–O demonstrates two different deconvoluted peaks referring to C=O of 37.6 at% and C—O of 62.4 at% (Figure S19c, Supporting Information). The configuration of OFGs and the proportion of the oxygen species in POC–O are analogous to

those of Co–POC–O, which are further confirmed by the identified C—O and —COOH species in the high-resolution carbon 1s XPS spectrum of POC–O (Figure S19d, Supporting Information). These experimental results manifest that POC–O is an OFGs modified carbon material without cobalt content or atomic Co–N_x–C sites.

Without the synergy of atomic Co–N_x–C sites, the POC–O electrocatalyst performs poorer ORR reactivity compared with Co–POC–O verified by lower potential of 0.67 V versus RHE at 1.0 mA cm^{-2}, lower limiting current, and higher Tafel slops of 46 mV $decade^{-1}$ (Figure 5a,b), suggesting that atomic Co–N_x–C sites are essential to the reactivity of oxygen reduction. In contrast, the selectivity for H_2O_2 electrosynthesis remains almost the same on the POC–O electrocatalyst as Co–POC–O (Figure 5c). Specifically, the selectivity at 0.7 V versus RHE is 80.2% for POC–O and 84.3% for Co–POC–O. Consequently, OFGs render high selectivity for two-electron oxygen reduction but requires atomic Co–N_x–C sites to improve the ORR reactivity for high-performance H_2O_2 electrosynthesis.

In order to further verify the contribution of atomic Co–N_x–C toward high ORR reactivity, chemical shielding of the cobalt content was conducted to restrict its functions. Thiocyanate ions (SCN^-) are commonly used as the inhibitor for transition metal ions because of the ultrahigh stability constant of thiocyanate-coordinated complexes.[29] After the addition of KSCN into the electrolyte, Co–POC–O exhibits an increased overpotential, a declined limiting current in the LSV curves (Figure S20, Supporting Information), and a higher Tafel slop of 47 mV $decade^{-1}$ (Figure S21, Supporting Information). These results indicate an obvious loss in the reactivity of oxygen reduction after blocking Co–N_x–C sites. However, as shown in Figure S22 (Supporting Information), the selectivity of H_2O_2 production is of ignorable change. Therefore, the shielding experiment additionally demonstrates that Co–N_x–C mainly contributes to the reactivity for oxygen reduction while the selectivity of H_2O_2 electrosynthesis is attributed to OFGs rather than Co–N_x–C.

Considering the above mechanism study based on control samples, we proposed a synergistic strategy for the rational design of noble-metal-free electrocatalyst with high-reactivity and high-selectivity simultaneously achieved for H_2O_2 electrochemical production. As is exhibited in Figure 5d, the Co–POC–R electrocatalyst with only atomic Co–N_x–C sites affords ideal ORR reactivity but poor selectivity for the two-electron pathway. As for the POC–O electrocatalyst with abundant OFGs but without atomic Co–N_x–C sites, the H_2O_2 selectivity is high but the inferior ORR reactivity limits the electrosynthetic efficiency. Therefore, simplex active site cannot satisfy multiple targets or meet the demand of complex processes, for instance, H_2O_2 electrosynthesis in our work. By comodification of atomic Co–N_x–C sites and OFGs responsible for ORR reactivity and two-electron pathway selectivity, respectively, the two active sites synergistically contribute to the electrocatalytic H_2O_2 production to render significantly improved H_2O_2 productivity (Figure S23, Supporting Information).

In order to further prove the practical performance of H_2O_2 electrosynthesis using the Co–POC–O electrocatalyst, the actual concentration of H_2O_2 was measured to identify the accumulation of H_2O_2 in the electrolyte. After electrolyzing for 90 min at a constant current of 100 mA, the H_2O_2 concentration can be easily accumulated to 1220 mg L^{-1} with the H_2O_2 production rate of 813 mg L^{-1} h^{-1} (Figure S24, Supporting Information). The faradaic efficiency is 64.1%, which is attributed to partial H_2O_2 decomposition on the platinum counter electrode. Therefore, the Co–POC–O electrocatalyst serves as a promising candidate for H_2O_2 electrosynthesis with high yield and efficiency.

In summary, a synergistic strategy is proposed for the design and fabrication of noble-metal-free electrocatalysts for high-performance H_2O_2 electrosynthesis. The atomic Co–N_x–C sites and oxygen functional groups comodified carbon-based electrocatalyst (Co–POC–O) was synthesized by pyrolysis and oxidization of the cobalt-coordinated framework porphyrin precursor. Both atomically dispersed Co–N_x–C sites and OFGs were unambiguously identified in Co–POC–O using comprehensive characterizations. The Co–POC–O electrocatalyst exhibits a remarkable performance for H_2O_2 electrochemical synthesis with high reactivity to afford a high potential at 1 mA cm^{-2} of 0.79 V versus RHE, high selectivity over 80%, and excellent stability. Furthermore, mechanism study on the synergistic effect of atomic Co–N_x–C sites and OFGs was performed to verify the atomic Co–N_x–C sites and OFGs contribute to the reactivity and selectivity for H_2O_2 electrosynthesis, respectively. This contribution not only affords rational design principles to fabricate high-performance H_2O_2 electrocatalysts as a demonstration of green chemistry, but also the strategy of endowing advanced materials with multiple active sites for the synthesis of important chemicals in a green and sustainable way.

Supporting Information

Supporting Information is available from the Wiley Online Library or from the author.

Acknowledgements

B.-Q.L. and C.-X.Z. contributed equally to this work. This work was supported by National Key Research and Development Program (2016YFA0202500 and 2016YFA0200101), Natural Scientific Foundation of China (21825501), and Tsinghua University Initiative Scientific Research Program. We thank Jin Xie, Dr. Cheng Tang, Dr. Hao-Fan Wang, and Dr. Bin Wang for helpful discussion.

Conflict of Interest

The authors declare no conflict of interest.

Keywords

energy electrocatalysis, hydrogen peroxide electrosynthesis, noble-metal-free electrocatalysts, oxygen reduction reaction, synergistic strategy

Received: December 19, 2018
Revised: March 11, 2019
Published online:

[1] a) I. Yamanaka, T. Murayama, *Angew. Chem., Int. Ed.* **2008**, *47*, 1900; b) X. Shi, S. Siahrostami, G.-L. Li, Y. Zhang, P. Chakthranont, F. Studt, T. F. Jaramillo, X. Zheng, J. K. Norskov, *Nat. Commun.* **2017**, *8*, 701.

[2] a) M. Xing, W. Xu, C. Dong, Y. Bai, J. Zeng, Y. Zhou, J. Zhang, Y. Yin, *Chem* **2018**, *4*, 1359; b) V. R. Choudhary, P. Jana, S. K. Bhargava, *Catal. Commun.* **2007**, *8*, 811.
[3] J. K. Edwards, B. Solsona, E. N. N, A. F. Carley, A. A. Herzing, C. J. Kiely, G. J. Hutchings, *Science* **2009**, *323*, 1037.
[4] J. M. Campos-Martin, G. Blanco-Brieva, J. L. G. Fierro, *Angew. Chem., Int. Ed.* **2006**, *45*, 6962.
[5] a) X. Cui, C. Tang, Q. Zhang, *Adv. Energy Mater.* **2018**, *8*, 1800369; b) Z. Weng, Y. Wu, M. Wang, J. Jiang, K. Yang, S. Huo, X.-F. Wang, Q. Ma, G. W. Brudvig, V. S. Batista, Y. Liang, Z. Feng, H. Wang, *Nat. Commun.* **2018**, *9*, 415; c) C. Tang, R. Zhang, W. Lu, L. He, X. Jiang, A. M. Asiri, X. Sun, *Adv. Mater.* **2017**, *29*, 1602441.
[6] a) S. Yang, A. Verdaguer-Casadevall, L. Arnarson, L. Silvio, V. Colic, R. Frydendal, J. Rossmeisl, I. Chorkendorff, I. E. L. Stephens, *ACS Catal.* **2018**, *8*, 4064; b) J. C. Byers, A. G. Gueell, P. R. Unwin, *J. Am. Chem. Soc.* **2014**, *136*, 11252.
[7] K. N. Wood, R. O'Hayre, S. Pylypenko, *Energy Environ. Sci.* **2014**, *7*, 1212.
[8] C. Zhang, X. Zou, Z. Du, J. Gu, S. Li, B. Li, S. Yang, *Small* **2018**, *14*, 1703960.
[9] C.-Y. Chen, C. Tang, H.-F. Wang, C.-M. Chen, X. Zhang, X. Huang, Q. Zhang, *ChemSusChem* **2016**, *9*, 1194.
[10] S. Siahrostami, A. Verdaguer-Casadevall, M. Karamad, D. Deiana, P. Malacrida, B. Wickman, M. Escudero-Escribano, E. A. Paoli, R. Frydendal, T. W. Hansen, I. Chorkendorff, I. E. L. Stephens, J. Rossmeisl, *Nat. Mater.* **2013**, *12*, 1137.
[11] J. S. Jirkovsky, I. Panas, E. Ahlberg, M. Halasa, S. Romani, D. J. Schiffrin, *J. Am. Chem. Soc.* **2011**, *133*, 19432.
[12] a) C. Tang, H.-F. Wang, X. Chen, B.-Q. Li, T.-Z. Hou, B. Zhang, Q. Zhang, M.-M. Titirici, F. Wei, *Adv. Mater.* **2016**, *28*, 6845; b) G.-L. Tian, M.-Q. Zhao, D. Yu, X.-Y. Kong, J.-Q. Huang, Q. Zhang, F. Wei, *Small* **2014**, *10*, 2251; c) E. Mitraka, M. Gryszel, M. Vagin, M. J. Jafari, A. Singh, M. Warczak, M. Mitrakas, M. Berggren, T. Ederth, I. Zozoulenko, X. Crispin, E. D. Glowacki, *Adv. Sustainable Syst.* **2019**, *3*, 1800110; d) M. Y. Vagin, I. Jeerapan, R. Wannapob, P. Thavarungkul, P. Kanatharana, N. Anwar, T. McCormac, M. Eriksson, A. P. P. Turner, E. W. H. Jager, W. C. Mak, *Electrochim. Acta* **2016**, *190*, 495.
[13] a) J. Park, Y. Nabae, T. Hayakawa, M.-a. Kakimoto, *ACS Catal.* **2014**, *4*, 3749; b) T.-P. Fellinger, F. Hasche, P. Strasser, M. Antonietti, *J. Am. Chem. Soc.* **2012**, *134*, 4072; c) F. Hasche, M. Oezaslan, P. Strasser, T.-P. Fellinger, *J. Energy Chem.* **2016**, *25*, 251; d) V. Perazzolo, C. Durante, R. Pilot, A. Paduano, J. Zheng, G. A. Rizzi, A. Martucci, G. Granozzi, A. Gennaro, *Carbon* **2015**, *95*, 949.
[14] a) Y. Liu, X. Quan, X. Fan, H. Wang, S. Chen, *Angew. Chem., Int. Ed.* **2015**, *54*, 6837; b) S. Chen, Z. Chen, S. Siahrostami, T. R. Kim, D. Nordlund, D. Sokaras, S. Nowak, J. W. F. To, D. Higgins, R. Sinclair, J. K. Norskov, T. F. Jaramillo, Z. Bao, *ACS Sustainable Chem. Eng.* **2018**, *6*, 311.
[15] a) C. Zhu, Q. Shi, B. Z. Xu, S. Fu, G. Wan, C. Yang, S. Yao, J. Song, H. Zhou, D. Du, S. P. Beckman, D. Su, Y. Lin, *Adv. Energy Mater.* **2018**, *8*, 1801956; b) F. Meng, H. Zhong, D. Bao, J. Yan, X. Zhang, *J. Am. Chem. Soc.* **2016**, *138*, 10226; c) X. Cui, S. Yang, X. Yan, J. Leng, S. Shuang, P. M. Ajayan, Z. Zhang, *Adv. Funct. Mater.* **2016**, *26*, 5708; d) Y. Chen, S. Ji, Y. Wang, J. Dong, W. Chen, Z. Li, R. Shen, L. Zheng, Z. Zhuang, D. Wang, Y. Li, *Angew. Chem., Int. Ed.* **2017**, *56*, 6937.
[16] a) Z. Lu, G. Chen, S. Siahrostami, Z. Chen, K. Liu, J. Xie, L. Liao, T. Wu, D. Lin, Y. Liu, T. F. Jaramillo, J. K. Norskov, Y. Cui, *Nat. Catal.* **2018**, *1*, 156; b) A. Moraes, M. H. M. T. Assumpcao, F. C. Simoes, V. S. Antonin, M. R. V. Lanza, P. Hammer, M. C. Santos, *Electrocatalysis* **2016**, *7*, 60.
[17] H. Wang, R. Cote, G. Faubert, D. Guay, J. P. Dodelet, *J. Phys. Chem. B* **1999**, *103*, 2042.
[18] A. Khataee, S. Sajjadi, S. R. Pouran, A. Hasanzadeh, S. W. Joo, *Electrochim. Acta* **2017**, *244*, 38.
[19] M. Zhang, Q. Dai, H. Zheng, M. Chen, L. Dai, *Adv. Mater.* **2018**, *30*, 1705431.
[20] a) C. Tang, B. Wang, H.-F. Wang, Q. Zhang, *Adv. Mater.* **2017**, *29*, 1703185; b) P. Chen, T. Zhou, L. Xing, K. Xu, Y. Tong, H. Xie, L. Zhang, W. Yan, W. Chu, C. Wu, Y. Xie, *Angew. Chem., Int. Ed.* **2017**, *56*, 610.
[21] a) Y. Han, Y.-G. Wang, W. Chen, R. Xu, L. Zheng, J. Zhang, J. Luo, R.-A. Shen, Y. Zhu, W.-C. Cheong, C. Chen, Q. Peng, D. Wang, Y. Li, *J. Am. Chem. Soc.* **2017**, *139*, 17269; b) G. Wu, K. L. More, C. M. Johnston, P. Zelenay, *Science* **2011**, *332*, 443.
[22] B.-Q. Li, S.-Y. Zhang, L. Kong, H.-J. Peng, Q. Zhang, *Adv. Mater.* **2018**, *30*, 1707483.
[23] B.-Q. Li, S.-Y. Zhang, B. Wang, Z.-J. Xia, C. Tang, Q. Zhang, *Energy Environ. Sci.* **2018**, *11*, 1723.
[24] Y. Qian, Z. Liu, H. Zhang, P. Wu, C. Cai, *ACS Appl. Mater. Interfaces* **2016**, *8*, 32875.
[25] Y. Guo, P. Yuan, J. Zhang, Y. Hu, I. S. Amiinu, X. Wang, J. Zhou, H. Xia, Z. Song, Q. Xu, S. Mu, *ACS Nano* **2018**, *12*, 1894.
[26] S. Kundu, Y. Wang, W. Xia, M. Muhler, *J. Phys. Chem. C* **2008**, *112*, 16869.
[27] Y. Wang, Y. Shao, D. W. Matson, J. Li, Y. Lin, *ACS Nano* **2010**, *4*, 1790.
[28] a) W. R. P. Barros, Q. Wei, G. Zhang, S. Sun, M. R. V. Lanza, A. C. Tavares, *Electrochim. Acta* **2015**, *162*, 263; b) M. H. M. T. Assumpcao, R. F. B. De Souza, D. C. Rascio, J. C. M. Silva, M. L. Calegaro, I. Gaubeur, T. R. L. C. Paixao, P. Hammer, M. R. V. Lanza, M. C. Santos, *Carbon* **2011**, *49*, 2842; c) M. E. M. Buan, N. Muthuswamy, J. C. Walmsley, D. Chen, M. Ronning, *Carbon* **2016**, *101*, 191; d) A. Bonakdarpour, D. Esau, H. Cheng, A. Wang, E. Gyenge, D. P. Wilkinson, *Electrochim. Acta* **2011**, *56*, 9074; e) M. Campos, W. Siriwatcharapiboon, R. J. Potter, S. L. Horswell, *Catal. Today* **2013**, *202*, 135.
[29] a) X. Song, L. Guo, X. Liao, J. Liu, J. Sun, X. Li, *Small* **2017**, *13*, 1700238; b) H.-W. Liang, S. Brueller, R. Dong, J. Zhang, X. Feng, K. Muellen, *Nat. Commun.* **2015**, *6*, 7992; c) L.-B. Lv, T.-N. Ye, L.-H. Gong, K.-X. Wang, J. Su, X.-H. Li, J.-S. Chen, *Chem. Mater.* **2015**, *27*, 544.